Improved cross-range resolution in TOPSAR imaging using Sentinel-1A in bistatic operation

Virginie Kubica*†, Xavier Neyt* and Hugh Griffiths†
*Dept. of Electrical Engineering, Royal Military Academy, Belgium
†Dept. of Electronic and Electrical Engineering, University College London, UK
Virginie.Kubica@elec.rma.ac.be
Xavier.Neyt@elec.rma.ac.be
Hugh.Griffiths@ucl.ac.uk

***Abstract*—Wide-swath SAR imaging modes such as ScanSAR or TOPSAR offer synoptic observations of large-scale phenomena with a high revisit frequency at the expense of a degraded cross-range resolution. In the bistatic configuration using a SAR satellite as illuminator of opportunity and a ground-based stationary receiver close to the imaged area, this poor cross-range resolution can be improved in some favourable geometries by exploiting the sidelobe emissions of the beams illuminating the adjacent sub-swaths. This has been already demonstrated for ScanSAR mode while this paper analyzes in detail the TOPSAR mode based on measurements of ESA's recently launched satellite Sentinel-1A.**

I. Introduction

The revisit time and the ability to make synoptic observations have made wide-swath SAR imaging modes the default mode of many radar satellites. One of the most important wide-swath modes is the ScanSAR mode [1] which was first implemented on Radarsat-1. Since then, other SAR satellites such as ESA's Envisat, Radarsat-2 and Japan's ALOS Phased Array L-band SAR (PALSAR) instruments were also ScanSAR operable. ScanSAR operating satellites image wide swaths by sweeping the antenna beam sequentially from near range to far range. To alleviate the drawbacks of the ScanSAR mode, such as the well-known scalloping effect, another wide-swath mode, called TOPSAR (Terrain Observation with Progressive Scans SAR) imaging mode, has been first discussed in [2] and is now the main mode of operation for ESA's recently launched satellite Sentinel-1A. While in the ScanSAR mode the antenna is steered only in the range direction, in TOPSAR mode, the antenna is steered in both azimuth and range. Those burst-modes allow imaging of a swath much wider than range ambiguity limits would normally allow but at the cost of degraded cross-range resolution. Table I draws up a non-exhaustive list of wide-swath modes implemented on SAR satellites and their monostatic spatial resolution. One can see that the TOPSAR imaging mode implemented on Sentinel-1A [3] is characterized by an imbalance between the range and the cross-range resolution which means that improving this coarse cross-range resolution thanks to a bistatic configuration is valuable.

The specific case of passive bistatic radar using a spaceborne transmitter and a stationary ground-based receiver, has already been examined [4]–[8] but the analysis is limited to the conventional Stripmap mode of radar satellites. The occurrence of satellite passes in Stripmap high-resolution mode is however not as frequent as passes in wide-swath mode [9]. Exploiting the favourable TOPSAR illuminations will therefore result in an increase in opportunities to obtain high-resolution SAR images.

TABLE I
A non-exhaustive list of wide-swath imaging satellites and their monostatic spatial resolution.

Radar satellites	Mode	Range resolution (m)	Cross-range resolution (m)
ASAR Envisat	ScanSAR WS	150	150
	ScanSAR GM	1000	1000
Radarsat-2	ScanSAR narrow (A/B)	$37.7 - 79.9$	60
	ScanSAR wide (A/B)	$72.1 - 160$	100
Sentinel-1A	TOPSAR IW	$2.7 - 3.5$	22
	TOPSAR EW	$7.9 - 15$	43

In [10], it was demonstrated that the coarse monostatic cross-range resolution of ScanSAR mode can be enhanced in the case of a bistatic configuration with a receiver close to the imaged area by exploiting the sidelobe emissions of the beams illuminating the adjacent sub-swaths. This method can restore the cross-range resolution of the Stripmap mode provided that the amplitude of the signals transmitted in the sidelobes of the ScanSAR beams is sufficient. This is the case in geometries for which the sidelobe radiations of the ScanSAR beams which illuminate the adjacent sub-swaths also illuminate the sub-swath in which the receiver and the imaged area are located. This can occur when the receiver and the imaged area are at the centre of the global swath. In this paper, the performance of the method are assessed in the case of TOPSAR illuminations.

The remainder of the paper is organized as follows. Section II draws up a comparison between ScanSAR and TOPSAR imaging modes in first the classical monostatic geometry and then in bistatic operation. In Section III, the cross-range resolution enhancement method [10] is reviewed and discussed in the case of TOPSAR imaging using first simulated data and then, Sentinel-1A real measurements. Finally, the conclusion is presented in Section IV.

II. Wide-swath modes in bistatic operation

The passive radar system investigated in this work consists of a space-based radar as illuminator of opportunity and a stationary ground-based receiver [11]. The spaceborne radar operates in one of the wide-swath imaging modes, i.e. ScanSAR (Fig. 1) or TOPSAR (Fig. 2), where the antenna beam is electronically steered to different contiguous range sub-swaths. In ScanSAR mode, each sub-swath is illuminated by the antenna beam for a short time interval, called burst duration, T_B, which is very small compared to T_F, the antenna-footprint time. T_R is the scan repeat time which is the time for the beam to come back to the same range sub-swath.

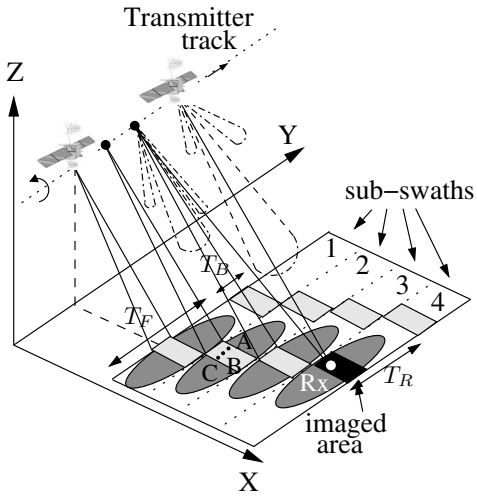

Fig. 1. Bistatic acquisition geometry in ScanSAR imaging mode in the case of four sub-swaths. The receiver and the imaged area are located at the edge of the global swath (dark area) and are illuminated by the sidelobes of the beam illuminating sub-swath 3 and afterwards, by the mainlobe of the beam illuminating sub-swath 4.

In TOPSAR mode, in addition to the range scanning, the antenna beam is steered during the illumination of each sub-swath from back to fore, i.e. in the opposite direction of spotlight mode. This azimuth scanning, illustrated on Fig. 2, results in a virtual shrinking of the Azimuth Antenna Pattern (AAP) [12] as seen by an on-ground target. Opposite to the ScanSAR mode, the burst duration, T_B, in TOPSAR mode is longer and is almost equal to the footprint time to ensure a sufficient dwell-time on target.

On Fig. 1 and 2, three pointlike scatterers, A, B and C, having the same slant range of closest approach to the transmitter but located at different azimuths are represented. To compare both wide-swath modes, the slow time - Doppler frequency diagrams are represented on Fig. 3 and 4. The Doppler histories of the targets are shown by dashed lines with the same negative slopes, equal to the Doppler rate k_r. Figure 3 illustrates the evolution of the Doppler frequency as a function of the slow time for a four sub-swath ScanSAR mode such as the ScanSAR Wide mode B (SWB) of Radarsat-2. In ScanSAR and in the monostatic geometry, the dwell-time, T_D, i.e. the azimuth integration time for a point target,

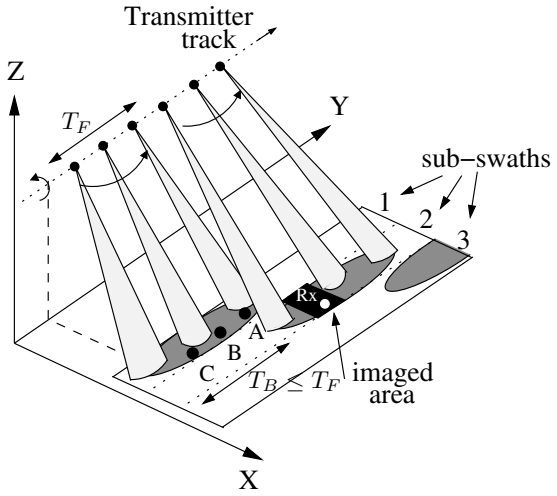

Fig. 2. Bistatic acquisition geometry in TOPSAR imaging mode in the case of three sub-swaths.

is identical to the burst time, T_B. The AAP, represented on the left on Fig. 3 as a bell-shape, is fixed in azimuth. The targets are illuminated by different portions of the AAP. This results in different amplitude weighting of the phase history of the different targets. A scalloping effect, a well-known regular azimuth modulation in the final SAR image follows [2].

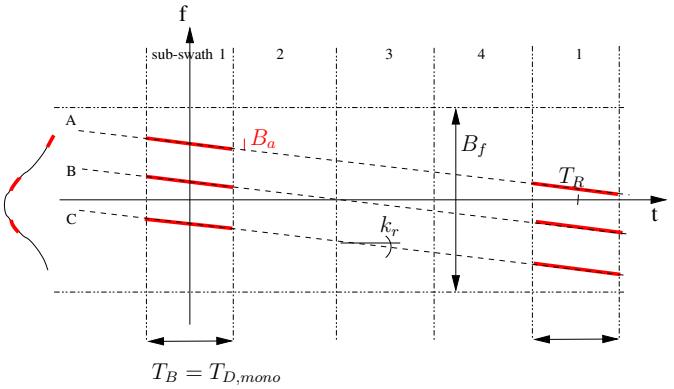

Fig. 3. ScanSAR mode: Time-frequency diagram of three scatterers in the monostatic geometry where B_f is the footprint bandwidth and $B_a = T_B k_r$ is the bandwidth for each target. The thick red lines represent the focused phase history.

Figure 4 illustrates the time-frequency diagram for a three sub-swath TOPSAR mode such as the Interferometric Wide-swath mode (IW) of Sentinel-1A. In this radar mode, each illuminated target experiences nearly the same AAP (blue dashed-line on Fig. 4) during the burst duration T_B. This results in a reduction of the scalloping effect. In both wide-swath modes, the poor cross-range resolution compared to Stripmap imaging is caused by a shortened target illumination: ScanSAR illuminates target with a small portion of its AAP, while in TOPSAR, the shorter target illumination is due to the along-track sweeping of the antenna beam.

The specific bistatic geometry investigated in this work allows the receiving system to receive echoes issued from the

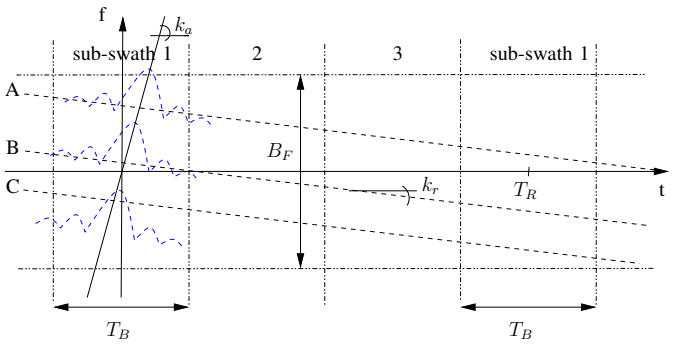

Fig. 4. TOPSAR mode: Time-frequency diagram of three scatterers in the monostatic geometry where the azimuth steering introduces a Doppler centroid rate k_a. The blue dashed lines represent the shrunk AAP.

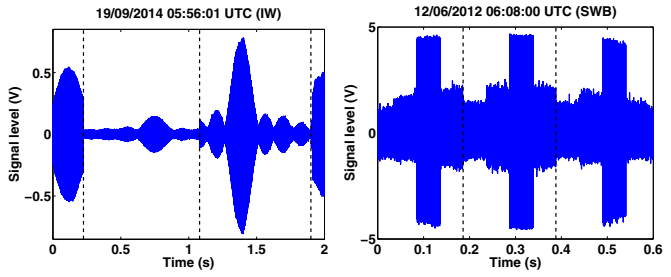

(a) (b)

Fig. 5. Acquired signals in wide-swath mode: (a) TOPSAR illumination of Sentinel-1A operating in IW mode defined by a burst duration of 0.82 sec and (b) 3 cycles of a ScanSAR illumination of Radarsat-2 operating in SWB with a burst duration of 0.05 sec.

sidelobes emissions of the adjacent beams from the transmitter. This is possible thanks to the short reflected path from the observed area and also because of the attenuation by the one-way transmit antenna gain pattern and not by the two-way antenna pattern. In this bistatic geometry, all scatterers in the small imaged area are illuminated approximately by the same AAP which extends on several sub-swaths on Fig. 3 and 4.

Figure 5 (a) depicts the acquired signal during an overpass of Sentinel-1A operating in IW mode over the ground-based receiving system in Brussels. The dashed lines demarcate the time interval spent by the beam on each sub-swath, T_B. Figure 5 (b) represents the received signal from Radarsat-2 operating in SWB mode characterized by 4 beams or sub-swaths. The dashed lines demarcate each group of 4 beams, T_R. In monostatic SAR, the burst duration equals the dwell-time on target, $T_{D,mono}$, and would be equal to 0.05 sec for SWB compared to a burst duration of 0.8 sec in TOPSAR mode and a dwell-time on target of 0.24 sec being the duration of the mainlobe of the shrunk AAP. This multiplication factor of 5 in dwell-time results in a better azimuth resolution of Sentinel-1A compared to Radarsat-2 as listed in Tab. I.

The amplitude of the transmitted pulses in both acquisitions is obviously determined by the azimuth antenna diagram of the transmitting antenna but also, for each beam, by the corresponding elevation antenna diagram at the elevation angle at which the receiver/scatterers are located.

III. Cross-range resolution enhancement method

After reviewing the method [10], the specific case of TOPSAR imaging will be discussed using first simulated data and then, real measurements.

A. Burst-mode SAR focusing

Let first define the signal model on which the cross-range resolution enhancement method is based. The imaged area consists of K ground patches. All measurement samples in time and space are stacked into a single measurement vector $\mathbf{y} \in \mathbb{C}^{\mathbf{MN\times 1}}$ with M the number of transmitted pulses and N the number of range cells. The total received signal is the sum of the responses from all ground patches and can be modeled as

$$\mathbf{y} = \mathbf{H_w x} + \mathbf{n} \tag{1}$$

where the k^{th} column of $\mathbf{H_w} \in \mathbb{C}^{\mathbf{MN\times K}}$ represents the signal that would be received from a scatterer located at ground patch k with a reflection coefficient of 1. The subscript in $\mathbf{H_w}$ refers to the azimuth modulation of the signal experienced by the imaged ground patch and illustrated in Fig. 5. The elements of the column vector $\mathbf{x} = [x^0, x^1, ..., x^k, ..., x^{K-1}]^T$ are the complex reflectivity of each ground patch and $\mathbf{n} \in \mathbb{C}^{\mathbf{MN\times 1}}$ denotes the thermal noise, assumed complex Gaussian. In the bistatic geometry considered in this work, each ground patch in the observed scene is assumed to experience the same AAP as the receiver since the imaged area is close to the receiver and small. Therefore, $\mathbf{H_w}$ can be rewritten as

$$\mathbf{H_w} = \mathbf{W} \odot \mathbf{H} \tag{2}$$

where $\odot$ denotes the Hadamard multiplication and the k^{th} column of matrix $\mathbf{H}$ has a unity constant amplitude and represents the signal that would be received from a scatterer located at ground patch k with a reflection coefficient of 1. The column of the matrix $\mathbf{W}$ are identical and equal to $\mathbf{w}$, the slow-time amplitude modulation which corresponds to the envelope of the signals shown on Fig. 5.

The unknown reflectivity vector $\mathbf{x}$ can be estimated by searching the maximum of its *a posteriori* probability density function (PDF) conditioned by the measurements or

$$\hat{\mathbf{x}} = \arg\max_{\mathbf{x}} p(\mathbf{x}|\mathbf{y}) \tag{3}$$

which can be reformulated with Bayes identity [13]

$$\hat{\mathbf{x}} = \arg\max_{\mathbf{x}} \frac{p(\mathbf{y}|\mathbf{x})p(\mathbf{x})}{p(\mathbf{y})} \tag{4}$$

Assuming a complex Gaussian distributed reflectivity and Gaussian noise, it is easily shown that the maximum is reached for [13]

$$\hat{\mathbf{x}} = \mathbf{R_x H_w^\dagger}(\mathbf{H_w R_x H_w^\dagger} + \mathbf{R_n})^{-1}\mathbf{y} \tag{5}$$

with $\mathbf{R_x} = E[\mathbf{x}\mathbf{x}^\dagger]$ being the covariance matrix of the scene reflectivity $\mathbf{x}$ and $\mathbf{R_n}$ that of the noise $\mathbf{n}$. In the Gaussian signal model, it is easily verified that the Maximum A Posteriori (MAP) estimator (5) is identical to the Minimum Mean Square Error (MMSE) estimator [14]. If $\mathbf{x}$ and $\mathbf{n}$ are assumed

Gaussian stationary processes, then the covariance matrices become $\mathbf{R_x} = \sigma_x^2\mathbf{I}$ and $\mathbf{R_n} = \sigma_n^2\mathbf{I}$ with σ_x^2 and σ_n^2 respectively the variance of the scene reflectivity and the noise. (5) can be rewritten as

$$\begin{aligned}\hat{\mathbf{x}} &= \mathbf{H_w^\dagger}(\mathbf{H_w}\mathbf{H_w^\dagger} + \vartheta\mathbf{I})^{-1}\mathbf{y} \\ &= \mathbf{H^\dagger}\mathbf{D^\dagger}(\mathbf{D}\mathbf{H}\mathbf{H^\dagger}\mathbf{D^\dagger} + \vartheta\mathbf{I})^{-1}\mathbf{y}\end{aligned} \tag{6}$$

with $\mathbf{H_w} = \mathbf{DH}$ and $\mathbf{D} \in \mathbb{R}^{MN\times MN}$ a diagonal matrix with $\mathbf{w}$ on its diagonal. In the case where $\mathbf{H}\mathbf{H}^\dagger$ is diagonal (with value K on its diagonal), i.e. if the number of pixels K is equal to the number of pulses M, (6) is finally equal to

$$\hat{\mathbf{x}} = \mathbf{H^\dagger}\mathbf{C_w}\mathbf{y} \tag{7}$$

where the matrix $\mathbf{C_w}$ is a diagonal matrix with the diagonal elements equal to

$$c_{w,i} = \frac{w_i}{w_i^2 K + \vartheta} \tag{8}$$

with w_i the i^{th} element of $\mathbf{w}$ and $\vartheta = \frac{\sigma_n^2}{\sigma_x^2}$ the inverse of the SNR. The matrix $\mathbf{C_w}$ acts as a compensation of the azimuth modulation embodied by $\mathbf{w}$. Therefore, this method consists in

- compensating the AAP modulation of the measurements (rightmost product)

$$\mathbf{y_c} = \mathbf{C_w}\mathbf{y} \tag{9}$$

- focusing using the conventional Matched Filter (MF) (leftmost product)

$$\hat{\mathbf{x}} = \mathbf{H^\dagger}\mathbf{y_c} \tag{10}$$

Note that the compensation (8) is optimum if the SNR embodied by ϑ is the true one. In reality, the SNR is not known and has to be estimated. The estimation of ϑ is very important as it defines how well the compensation of the azimuth modulation will happen. For an optimistic estimation of the SNR (ϑ too small), $\mathbf{c_w}$ tends to the inverse function of the azimuth modulation window $\mathbf{w}$, i.e. the signal as well as the noise will be compensated which results in an amplification of the noise. Whereas for a pessimistic estimation of the SNR (ϑ too large), neither the signal nor the noise are amplified. In other words, $\mathbf{c_w}$ strives to find a reasonable balance between, on the one hand, compensation of the weak signals and, on the other hand, amplification of the noise. In the sequel, the optimum value of ϑ is assumed known.

It was demonstrated in [10] that the noise amplification induced by the method does not strongly impact the SAR imaging if the pulses transmitted in the elevation sidelobes have sufficient SNR. This condition was easily met in ScanSAR mode for which the AAP is nearly constant within the burst duration. This is not the case in TOPSAR for which the sidelobes of the sinc-shaped azimuth pattern also illuminate the scene as illustrated in Fig. 5 (a). As a result, the aforementioned condition can be more difficult to meet in TOPSAR mode since the amplitude of the transmitted signals in the sidelobes can be very small.

B. Performance evaluation on simulated data

To give a quantitative insight of the performance of the method in a TOPSAR illumination, a scenario with a point scatterer in presence of noise is simulated by a Monte Carlo method (100 realizations). A Signal-to-Noise Ratio (SNR) of 20 dB after focusing is chosen. The simulated azimuth modulation is based on the measured Sentinel-1A signal envelope of Fig. 5 (a). Two extreme cases have been considered. First, a single-beam illumination (T_B = 0.8 sec for IW), as would be obtained for a receiver/scatterer at the very edge of the global swath, would result in a sinc-shaped azimuth modulation like the portion of the envelope of the signal between 1.08 sec and 1.9 sec on Fig. 5 (a). Secondly, if the receiver/scatterer are located in the center of the global swath, a multi-beam illumination occurs with an azimuth modulation equals to the entire slow-time envelope of Fig. 5 (a). Figure 6 shows cuts of the Impulse Response Function (IRF) along the bistatic isorange and as expected [15], an improved cross-range resolution results in the case of multi-beam illumination. If the preprocessing step (9) is applied, the cross-range resolution is kept while the sidelobe levels considerably decrease as shown on Fig. 6 (solid line).

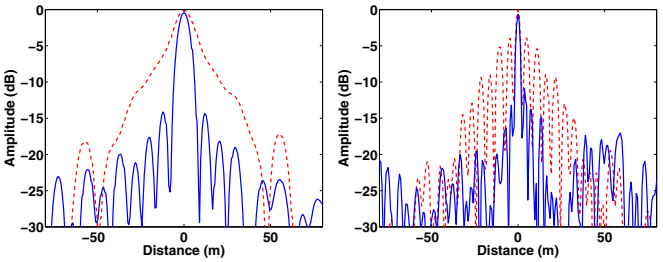

(a) (b)

Fig. 6. IRF cuts along the scatterer's isorange using the conventional MF (dashed line) and the cross-range resolution-enhancement method (solid line) in (a) a single-beam illumination and (b) a multi-beam illumination ($SNR =$ 20 dB after focusing).

To study the impact of the noise amplification induced by the method, the Mean Square Error (MSE) of the one-dimensional IRF profile (along the azimuth direction) is computed for increasing SNR. The case of a multi-beam illumination is considered. Figure 7 depicts the mean MSE with error bars representing one standard deviation on either side of the mean. For the conventional MF focusing (dashed line), the mean MSE is approximately constant for large SNRs while it decreases for increasing SNR if the cross-range compensation is applied. The mean MSE of the IRF of Fig. 6 (b) ($SNR = 20$ dB) is equal to 0.088 for the conventional MF and to 0.037 for the cross-range resolution-enhancement method. One can see that the cross-range resolution-enhancement method based on MMSE estimator outperforms the conventional MF as expected.

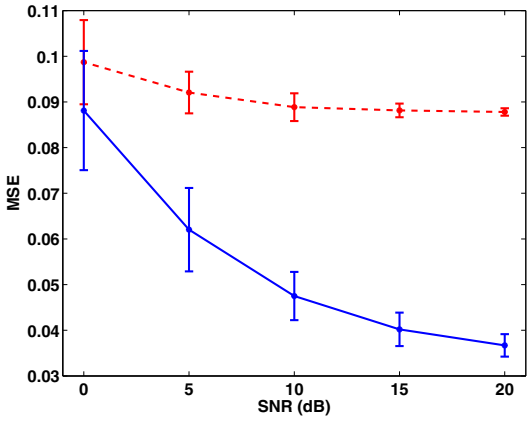

Fig. 7. Mean value of the MSE as a function of the SNR (after focusing) in the case of a multi-beam illumination using the conventional MF (dashed line) and the cross-range resolution-enhancement method (solid line). Error bars represent one standard deviation on either side of the mean.

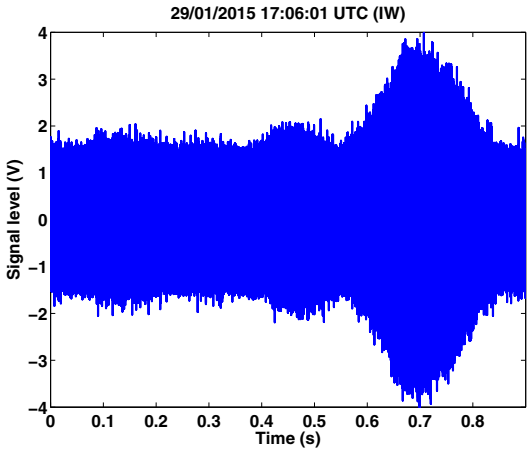

Fig. 8. Acquired signal during the illumination of the ground-based receiver located in Brussels on the 29^{th} of January 2015.

C. Performance evaluation on experimental data

On the 29^{th} of January 2015, the receiver, located in Brussels, was in the centre of the swath of Sentinel-1A operating in the TOPSAR IW mode. The 0.9-second acquired signal, shown on Fig. 8, represents the shrunk AAP illuminating the receiver and the surrounding area. The performance of the cross-range resolution enhancement method can be illustrated by analyzing point-like targets in the SAR image. Figures 9 and 10 show Single-Look Complex (SLC) georeferenced SAR images containing several point scatterers. Without any amplitude compensation method, each point scatterer has high sidelobes which could hide smaller scatterer as illustrated on Fig. 9. On Fig. 10, the sidelobes are reduced after application of the method and the point-like targets can be easily distinguished. This final result demonstrates that the cross-range resolution enhancement method can be applied in the case of a TOPSAR illumination for sufficient SNRs.

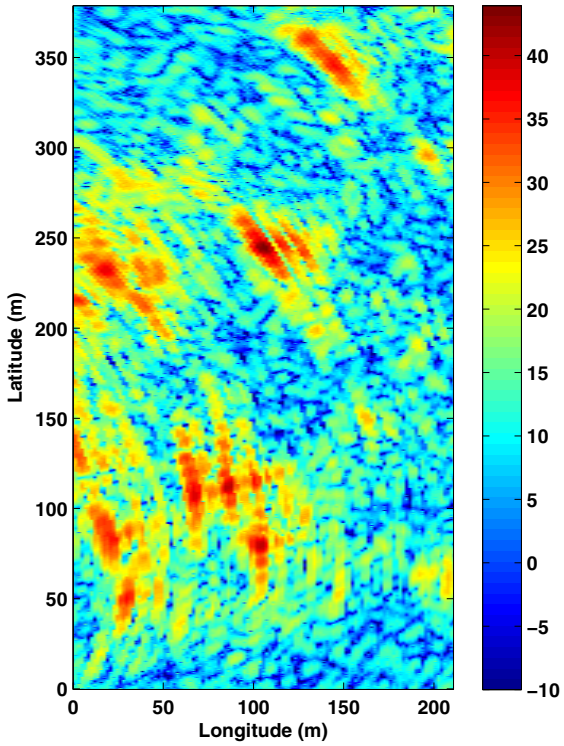

Fig. 9. Zoom on point scatterers in the georeferenced SAR image obtained with the conventional MF.

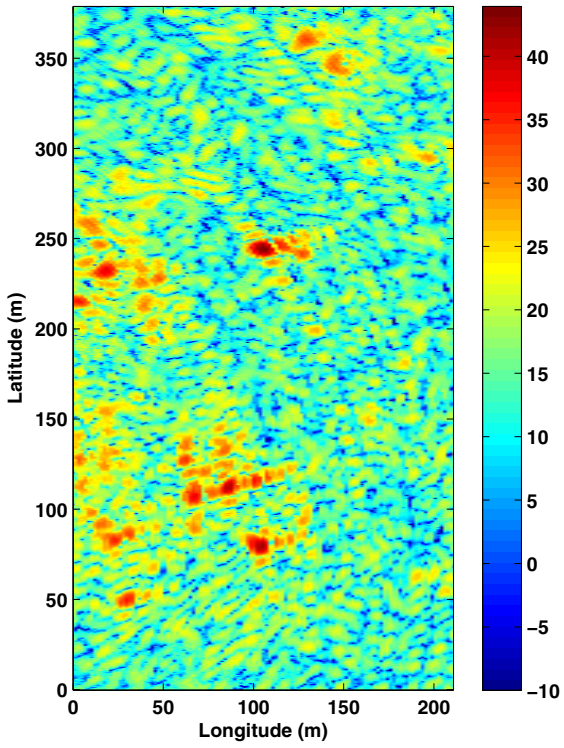

Fig. 10. Zoom on point scatterers in the georeferenced SAR image obtained with the cross-range resolution enhancement method.

IV. Conclusion

In this paper, we illustrate that, for sufficient SNRs, the coarse monostatic cross-range resolution of the TOPSAR imaging mode can be improved by considering a bistatic configuration with a receiver close to the imaged area. This bistatic geometry offers a longer illumination of the scene by the azimuth sidelobes of the shrunk AAP together with the beams illuminating the adjacent sub-swaths. The cross-range resolution-enhancement method is even more valuable in TOPSAR mode compared to ScanSAR mode as the range resolution in TOPSAR is very good. Besides, exploiting TOPSAR mode illuminations in addition to ScanSAR mode illuminations in the bistatic geometry studied in this work will significantly increase the opportunity to produce high cross-range resolution SAR images. As an example, the European Space Agency announces a two-day revisit time [9] of the constellation of Sentinel-1 satellites (A and B) in Europe which is calculated considering a low cross-range resolution Wide-swath mode.

References

[1] R. Raney, A. Luscombe, E. Langham, and S. Ahmed, "RADARSAT," *Proceedings of the IEEE*, vol. 79, pp. 839–849, June 1991.

[2] F. De Zan and A. Monti Guarnieri, "TOPSAR: Terrain Observation by Progressive Scans," *IEEE Transactions on Geoscience and Remote Sensing*, vol. 44, no. 9, pp. 2352–2360, 2006.

[3] C. Thain, R. Barstow, and T. Wong, "Sentinel-1 Product Specification," tech. rep., MDA, 2011.

[4] J. Sanz-Marcos, P. Lopez-Decker, J. J. Mallorqui, A. Aguasca, and P. Prats, "SABRINA: A SAR Bistatic Receiver for Interferometric Applications," *IEEE Geoscience and Remote Sensing Letters*, vol. 4, pp. 307–311, Apr. 2007.

[5] A. P. Whitewood, C. J. Baker, and H. D. Griffiths, "Bistatic Radar Using Spaceborne Illuminator," in *Proceedings of IET International Conference on Radar Systems*, (Edinburgh, UK), Oct. 2007.

[6] P. Samczynski and K. Kulpa, "Passive SAR imaging using a satellite pulsed radar as an illuminator of opportunity," in *Radar Symposium (IRS)*, (Berlin, Germany), pp. 157–161, 2012.

[7] F. Behner and S. Reuter, "Hitchhiker, Hybrid Bistatic High Resolution SAR experiment using a Stationary Receiver and TerraSAR-X Transmitter," in *Proc. of the 8th European Conference on Synthetic Aperture Radar*, (Aachen, Germany), pp. 1030–1033, 2010.

[8] R. Wang, Y. Deng, Z. Zhang, Y. Shao, J. Hou, G. Liu, and X. Wu, "Double-Channel Bistatic SAR System With Spaceborne Illuminator for 2-D and 3-D SAR Remote Sensing," *IEEE Transactions on Geoscience and Remote Sensing*, vol. 51, pp. 4496–4507, Aug. 2013.

[9] "ESA's radar observatory mission for GMES operational services," *ESA Special Publication*, no. 1322/1, 2012.

[10] V. Kubica and X. Neyt, "Feasibility of resolution-enhanced burst-mode interferometry in bistatic SAR," in *Proceedings of IEEE Conference on Radar*, (Adelaide, South Australia), Sept. 2013.

[11] E. Cristofani, V. Kubica, and X. Neyt, "A multibeam opportunistic SAR system," in *Proceedings of IEEE Radar Conference*, (Kansas City, MI), May 2011.

[12] D. D'Aria, D. Giudici, F. De Zan, A. M. Guarnieri, and F. Rocca, "Burst-mode SAR's for wide-swath surveys," *Canadian Journal of Remote Sensing*, vol. 33, pp. 27–38, 2007.

[13] H. Van Trees, *Detection, estimation and modulation theory — Part I*. John Wiley and Sons, 2001.

[14] S. M. Kay, *Fundamentals of statistical signal processing — Estimation theory*. Englewood Cliffs, NJ: Prentice-Hall, 1993.

[15] J. C. Curlander and R. N. McDonough, *Synthetic Aperture Radar, Systems and Signal Processing*. NY: John Wiley and Sons, 1991.